Edge-to-edge topological spectral transfer in diamond photonic lattices

Gabriel Cáceres-Aravena[†],[1,2] Bastián Real[†],[1,2] Diego Guzmán-Silva,[1,2] Paloma Vildoso,[1,2]
Ignacio Salinas,[1,2] Alberto Amo,[3] Tomoki Ozawa,[4] and Rodrigo A. Vicencio[1,2]

[1] *Departamento de Física, Facultad de Ciencias Físicas y Matemáticas, Universidad de Chile, Chile*
[2] *Millenium Institute for Research in Optics - MIRO, Universidad de Chile, Chile*
[3] *Univ. Lille, CNRS, UMR 8523—PhLAM—Physique des Lasers Atomes et Molécules, F-59000 Lille, France*
[4] *Advanced Institute for Materials Research (WPI-AIMR), Tohoku University, Sendai 980-8577, Japan*

(Dated: July 4, 2023)

TOPOLOGY OF THE DIMERIZED DIAMOND LATTICE

In the following, we explain the topology of the dimerized diamond lattice and how it is related to the Su-Schrieffer-Heeger (SSH) model. As written in Eq. (1) of the main text, the dynamics equation of the diamond lattice is

$$\begin{aligned} -i\partial_z A_n &= t_1 B_n + t_2 B_{n+1}\,, \\ -i\partial_z B_n &= t_1(A_n + C_n) + t_2(A_{n-1} + C_{n-1})\,, \\ -i\partial_z C_n &= t_1 B_n + t_2 B_{n+1}\,. \end{aligned} \tag{1}$$

One can notice that these equations are invariant under the exchange of A_n and C_n. Physically this symmetry corresponds to the inversion symmetry around the horizontal axis going through B sites. Moving to a basis where this inversion symmetry is diagonalized, the topology of the system becomes clearer. We can achieve this change of basis by defining

$$u_n \equiv \left(\frac{A_n + C_n}{\sqrt{2}}\right)$$

and

$$v_n \equiv \left(\frac{A_n - C_n}{\sqrt{2}}\right)\,.$$

Then, it is possible to obtain the following set of equations which are equivalent to the original ones:

$$\begin{aligned} -i\partial_z u_n &= \sqrt{2}t_1 B_n + \sqrt{2}t_2 B_{n+1}\,, \\ -i\partial_z B_n &= \sqrt{2}t_1 u_n + \sqrt{2}t_2 u_{n-1}\,, \\ -i\partial_z v_n &= 0\,. \end{aligned} \tag{2}$$

We see that the equation for v_n is completely decoupled from the equations for u_n and B_n. From this expression we notice that $u_n = B_n = 0$ for any n, namely $(A_n, B_n, C_n) = (1, 0, -1)/\sqrt{2}$, is a zero energy solution of Eq. (2), which is exactly the flat band eigenstate of the system. Furthermore, if we consider B_n and u_n to be two "sites" in a unit cell at position n, then the first two equations of Eq. (2) are of the form of the Su-Schrieffer-Heeger model with intra-cell coupling of $\sqrt{2}t_1$ and the inter-cell coupling of $\sqrt{2}t_2$. Therefore, the band structure becomes topological and there exist zero energy edge modes when $\delta = t_1/t_2 < 1$.

Finally, we note that for the topology to be well defined and nontrivial, the system needs the inversion and chiral symmetries. In our case, the inversion symmetry is obtained under the exchange of A_n and C_n sites and chiral symmetry is present due to no coupling between B_n or u_n themselves.

ORIGIN AND REGION OF EXISTENCE OF THE EDGE STATES

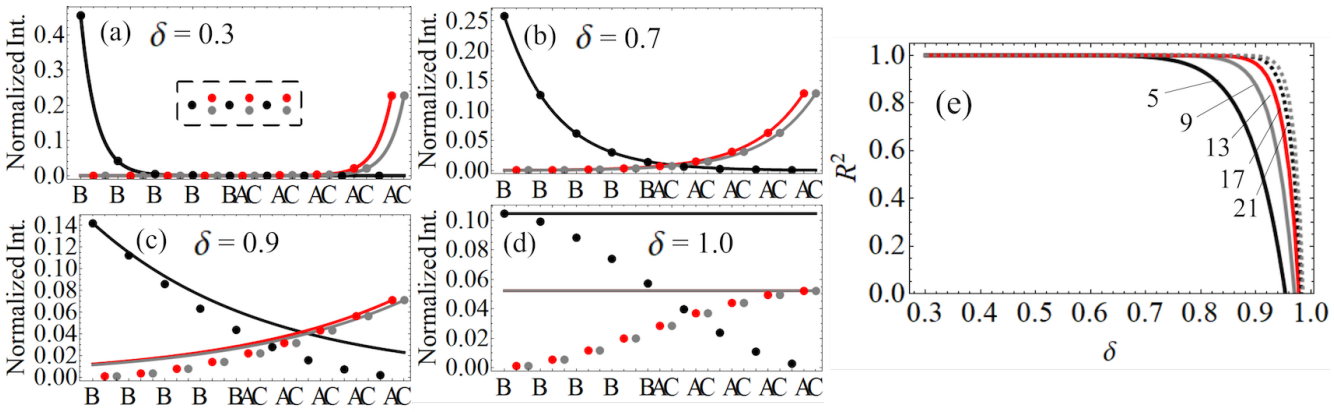

Figure S1. Edge states and exponencial decay. (a)-(d) Show the intensity profile of the edge states using the numerical calculation (dots) and the theoretical curve (continuos line), using 9 unit cells and for the cases $\delta = 0.3, 0.7, 0.9, 1.0$ respectively. (e) The coefficient R^2 vs δ for the case of 5 unit cells (black line), 9 unit cells (gray line), 13 unit cells (red line), 17 unit cells (black dashed line) and 21 unit cells (gray dashed line).

To understand the appearance of the edge states and verify in which condition these edge states exist, we use a plane wave approximation $(A_n(z), B_n(z), C_n(z)) = (a_n, b_n, c_n)e^{i\beta_z z}$ in Eq. (1), obtaining the following set of equations

$$\beta_z b_1 = t_1(a_1 + c_1) \,, \tag{3}$$
$$\beta_z a_1 = t_1 b_1 + t_2 b_2 \,,$$
$$\beta_z c_1 = t_1 b_1 + t_2 b_2 \,, \tag{4}$$
$$\beta_z b_2 = t_2(a_1 + c_1) + t_1(a_2 + c_2) \,, \tag{5}$$
$$\beta_z a_2 = t_1 b_2 + t_2 b_3 \,,$$
$$\beta_z c_2 = t_1 b_2 + t_2 b_3 \,, \tag{6}$$
$$\vdots = \vdots \,,$$
$$\beta_z b_n = t_2(a_{n-1} + c_{n-1}) + t_1(a_n + c_n) \,,$$
$$\beta_z a_n = t_1 b_n + t_2 b_{n+1} \,,$$
$$\beta_z c_n = t_1 b_n + t_2 b_{n+1} \,,$$
$$\vdots = \vdots \,,$$
$$\beta_z b_N = t_2(a_{N-1} + c_{N-1}) + t_1(a_N + c_N) \,, \tag{7}$$
$$\beta_z a_N = t_1 b_N \,,$$
$$\beta_z c_N = t_1 b_N \,. \tag{8}$$

Then, as an ansatz we use the energy of the eigenstate is $\beta_z = 0$, finding from Eq. (4) that $b_2/b_1 = -t_1/t_2 = -\delta$. Similarly, from Eq. (6) we find that $b_3/b_2 = -\delta$, and we can iterate this to obtain that $b_n/b_{n-1} = -\delta$. In this way, we find that the amplitude of the n-th b site of the edge state is given by

$$b_n = b_1(-\delta)^{n-1} \,, \tag{9}$$

and b_1 is a normalization constant. From the previous result we notice that as n increases $b_n \to 0$ when $\delta < 1$. But if $\delta > 1$ then $b_n \to \infty$, thus the solution (9) is only valid when $\delta < 1$. From Eq. (3) we find that $a_1 + c_1 = 0$ and from Eq. (5) we find that $a_2 + c_2 = 0$, and we can iterate this to obtain $a_n + c_n = 0$. This condition have two solutions: the flat band solution $a_n = -c_n$ or the amplitudes a_n and c_n are equal to zero. In both cases, the state exists. On the other edge, we use the condition in Eq. (8) and we obtain that $b_N = 0$ and from the Eq. (8) we find that $t_2(a_{N-1} + c_{N-1}) + t_1(a_N + c_N) = 0$, and this equation has two solutions: the flat band condition in which $a_n = -c_n$

and the dispersive band condition which is $a_n = c_n$. The solution of the flat band is trivial. On the other hand, the calculation of the dispersive condition leads to the following expression for the amplitudes of the a and c sites of the edge state:

$$a_n = a_N(-\delta)^{N-n} \quad , \quad c_n = c_N(-\delta)^{N-n} \, , \tag{10}$$

with $a_N = c_N$ constants of normalization. There is a topological transition in $\delta = 1$ so the previous theoretical expressions are only valid for $\delta < 1$. In the cases that δ is approaching to 1, the edge states evolve into bulk states. Therefore edge states should fit the theoretical expressions found in Eqs. (9) and (10) for small δ but not when δ approaches to 1.

In order to corroborate this result, we simulate numerically a lattice with 9 unit cells, and we calculate the eigenvalues and eigenstates of the system, and we plot the intensity in each site in because it is clearer to see the exponential decay of edge states and how they are related to experimental data. Figures S1.(a)-(d) show the intensity in sites a_n (in red), sites b_n (in black) and sites c_n i(n gray) for different values of δ. The continuous line is used for the theoretical expression shown in Eqs. (9) and (10), and dots are used for computed edge states. We observe that the theoretical curve fits the edge eigenstate pretty well for $\delta < 0.7$, however the fit fails at $\delta > 0.9$. In order to study this fit error we calculate the coefficient R^2 for different amount of unit cells and we plot the results in Fig.S1(e). We observe that for any number of unit cells the R^2 decreases as δ approaches to 1. However, the R^2 decrement is faster for smaller lattices. Negative values of R^2 indicate that there is no correlation between the theoretical expression and the computed eigenstate, for example Fig. S1(d). Using 9 unit cells we find that the $R^2(\delta = 0.7) = 0.99995$ and $R^2(\delta = 0.76) = 0.99926$. Therefore around $\delta = 0.7$ the approach decrease in quality.

SPECTRA FOR DIFFERENT SYSTEM SIZES

As mentioned in the main text, the lattice size affects the existence region of the edge states and the degeneracy of their eigenfrequencies. To better clarify this fact, Figure S2(a)-(c) show the spectra of the dimerized diamond lattices composed of (a) 5 unit cells, (b) 9 unit cells, and (c) 13 unit cells. We observe the eigenfrequencies of the edge states decrease to zero as $\delta \to 0$, being faster for bigger lattices. Figure S2(d) and (e) show clearly that the degeneracy of the edge states takes place at larger δ for a lattice with 13 unit cells (e) compared to a lattice with 5 unit cells (d).

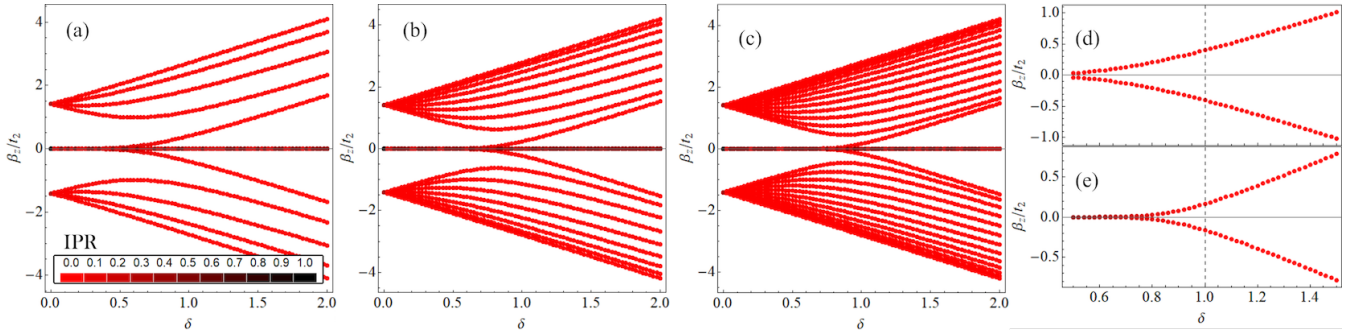

Figure S2. Spectrum of the dimerized diamond lattice. (a) The spectra with 5 unit cells, (b) 9 unit cells and (c) 13 unit cells. (d) The eigenvalues of the edge states for 5 unit cells, and (e) for 13 unit cells. $t_2 = 1$.

STATE TRANSFER FROM ONE EDGE TO THE OPPOSITE EDGE

Once the lattice gets finite, the eigenfrequencies of the edge states split apart and their amplitude profiles hybridize. Therefore, each eigenfrequency exhibits an edge state with amplitude on both boundaries. For example, Figure S3(a)-(d) show the amplitude of the eigenstate associated with negative [(a) and (c)] and positive [(b) and (d)] eigenvalues for a lattice with 9 unit cells and the indicated δ. We see that negative eigenvalues show an antibonding-like edge states, whereas positive values display a bonding-like edge states. Notice that all the profiles decay exponentially into the lattice bulk and this decay is longer as δ approaches to 1. Adding these eigenstates, we obtain an edge state completely localized in the left edge with amplitude only on B sites. If a given initial condition excites only one edge, an oscillatory pattern will appear due to the excitation of a sum of non-degenerate solutions.

To see this oscillation and topological transfer, we simulate a lattice with an initial condition given by the theoretical expression for the edge state $B_n = B_1(-\delta)^{n-1}$, and we expect that this initial condition should oscillate from one edge to the other. Figure S4(a) shows the simulation of the oscillation of the center of mass using 9 unit cells and $\delta = 0.7$. In Fig. S4(b)-(d) we plot the normalized intensity versus projected site at three different propagation distances, marked as a red circle, star and pentagon in Fig. S4(a). From these figures we notice clearly how the initial condition with light only in B sites (black dots) moves to a scenario where the light is only present in A and C (red and gray dots) sites.

We also notice that the difference between the eigenvalues of the edge states defined as $\Delta\beta_z^e = |\beta_{z,\text{Edge State 1}} - \beta_{z,\text{Edge State 2}}|$ and the frequency of oscillation of the center of mass ω are related by the expression $\Delta\beta_z^e = 2\pi/\omega$. This result is shown in Fig. S4(e) for different values of δ and taking in consideration three different cases: 5 unit cells (in black), 9 unit cell (in red) and 13 unit cells (in gray). The dots correspond to the calculation of $\Delta\beta_z^e$ using the oscillation of the center of mass and the lines to the use of the difference of eigenvalues. We observe a good agreement between both results. We also observe $\Delta\beta_z^e$ increases as δ increases and for a value of $\delta = 0.7$ (which is the one used in the main text) we have a value of $\Delta\beta_z^e$ close to 0.06.

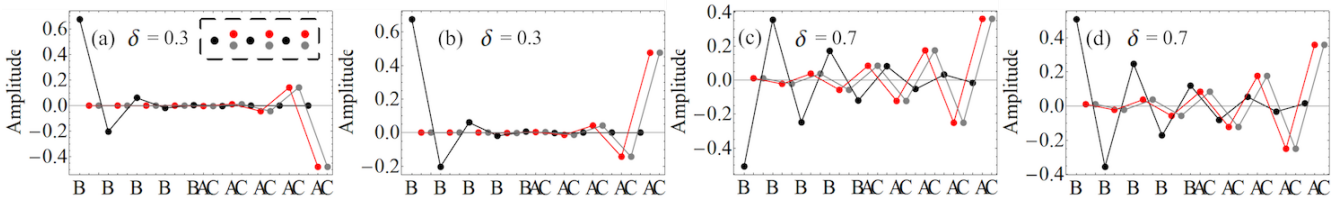

Figure S3. (a) The amplitude of the edge eigenstate for $\delta = 0.3$ with positive eigenvalue $\beta_z^{e+}/t_2 = 2.5\times10^{-5}$. (b) The eigenstate associated with the negative eigenvalue $\beta_z^{e-}/t_2 = -2.5\times10^{-5}$ with $\delta = 0.3$. The images (c) and (d) are the amplitude of the edge eigenstates positive and negative, respectively, with eigenvalue $|\beta_z/t_2| = 0.0293$. In black the b sites, in red the a sites and in gray the c sites.

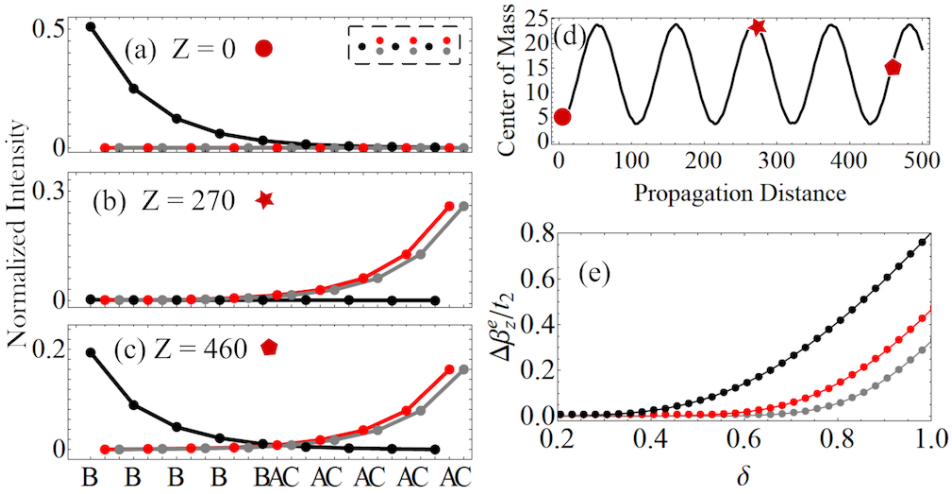

Figure S4. State transfer and center of mass. (a)-(c) Normalized intensity vs. site of unit cell for $z = 0$, $z = 270$ and $z = 460$, respectively. Black dots are used for B sites, red dots for A sites and gray dots for C sites. (d) Calculated center of mass using 9 unit cells and $\delta = 0.7$. The red marks represent different propagation distances used in (a)-(c). (e) Calculated $\Delta\beta_z^e$ using the oscillation frequency of the center of mass (dots) and the difference of eigenvalues of the edge states (continuos line), for the case of 5 unit cells (in black), 9 unit cells (in red) and 13 unit cells (in gray). $t_2 = 1$.

DIMERIZED DIAMOND LATTICE WITH NEXT-NEAREST-NEIGHBOR COUPLING

In this section we study the main impact of adding next-nearest-neighbor (NNN) couplings in the dimerized diamond lattice, which corresponds to the vertical coupling between A and C sites [see Fig. 1(a) main text]. Figure S5(b) shows the spectrum and Density of States (DOS) when this vertical coupling is taken into account ($V_v = 0.5t_2$). Comparing to the spectrum of the regular dimerized lattice (without NNN coupling) shown in Fig. S5(a), the flat band undergoes a frequency shift from $\beta_z/t_2 = 0$ to $\beta_z/t_2 = -V_v$, and the frequencies of the edge states are not degenerate. Specifically, the edge state with amplitudes on B sublattice remains at zero frequency, whereas the edge state with amplitudes on A and C sublattices shifts its frequency to $\beta_z/t_2 = V_v$. As a consequence, hybridization among the edge states does not occur in small-size lattices and the demonstrated transfer of the main text is not expected. Moreover, we also computed numerically the average beam displacement (m_d) [1] in this case, as shown in Fig. S5(c). Although chiral symmetry is broken when adding NNN couplings, the computed m_d exhibits a transition as $\delta = t_1/t_2$ is swept within the range [0, 2]. These numerical facts show that average beam displacement is still roughly quantized even in the presence of A-C coupling. More generally, following the recipe of Mong and Shivamoggi [2] one can define a bulk invariant relevant for the bulk-edge correspondence when A-C coupling is present, and this bulk invariant coincides with the winding number in the absence of A-C coupling, showing that bulk-boundary correspondence remains to hold in the presence A-C coupling.

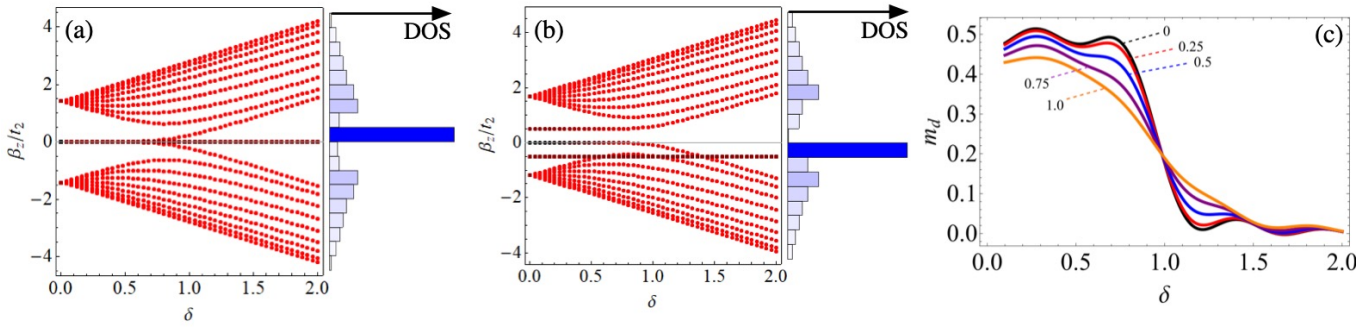

Figure S5. Dimerized diamond lattice with next-nearest-neighbor couplings. (a) and (b) Spectrum of a dimerized diamond lattice composed of nine unit cells without and with NNN couplings ($V_v = 0.5t_2$), respectively. Density of States for each case is plotted besides. (c) Average beam displacement computed numerically when considering vertical coupling between A and C sites, $V_v = 0$; $0.25t_2$; $0.5t_2$; $0.75t_2$; $1t_2$.

FABRICATION TECHNIQUE, COUPLING AND LATTICE CHARACTERIZATION

We fabricate several dimerized diamond photonic lattices, of 9 unit cells each, by using a femtosecond (fs) laser writing technique [3, 4], as it is sketched in Fig.1(c) of main text. Ultrashort pulses from a ATSEVA ANTAUS Yb-doped 1030 nm fiber laser, at a repetition rate of 500 kHz, are tightly focused on a $L_0 = 7$ cm long borosilicate glass wafer (with refractive index $n_0 = 1.48$). The laser pulses weakly modify the material properties at the illuminated region, inducing a permanent refractive index contrast of $\Delta n \approx 10^{-3}$ [5]. Straight waveguides are created by slowly translating the glass along the z coordinate by means of a motorized XYZ stage at a velocity of 0.4 mm/s. At a writing power of ~ 110 mW, each fabricated waveguide holds a single mode at 640 nm [5].

The fabrication of a diamond lattice demands a precise optimization of distances, in order to avoid second-order effects which could affect the observation of the tight-binding phenomenology, as described by model (1). For example, a non-negligible horizontal coupling in between A or C sites would simply destroys the FB as well as the chiral symmetry of edge localized states. Therefore, as we are using a long glass wafer, the distances in between lattice sites must be, in general, large enough to avoid next-nearest neighbor interactions.

In Fig. S6 we show a complete characterization of the 17 fabricated lattices, where vertical asymmetries have been corrected in the fabrication process. In this first experiment, the horizontal total distance was set to $d_1 + d_2 = 60$ μm to avoid next-nearest neighbor coupling. At the first column we observe the lattice distances and microscope images of two unit cells. Then, we show output intensity images, taken at 640 nm, for different input conditions: B-left edge site (C1M), 5-th unit cell B-site (C5M), C-right edge site (C9B), A-right edge site (C9T), A and C right edge equal phase sites (In-phase), and A and C right edge out of phase sites (Out-phase).

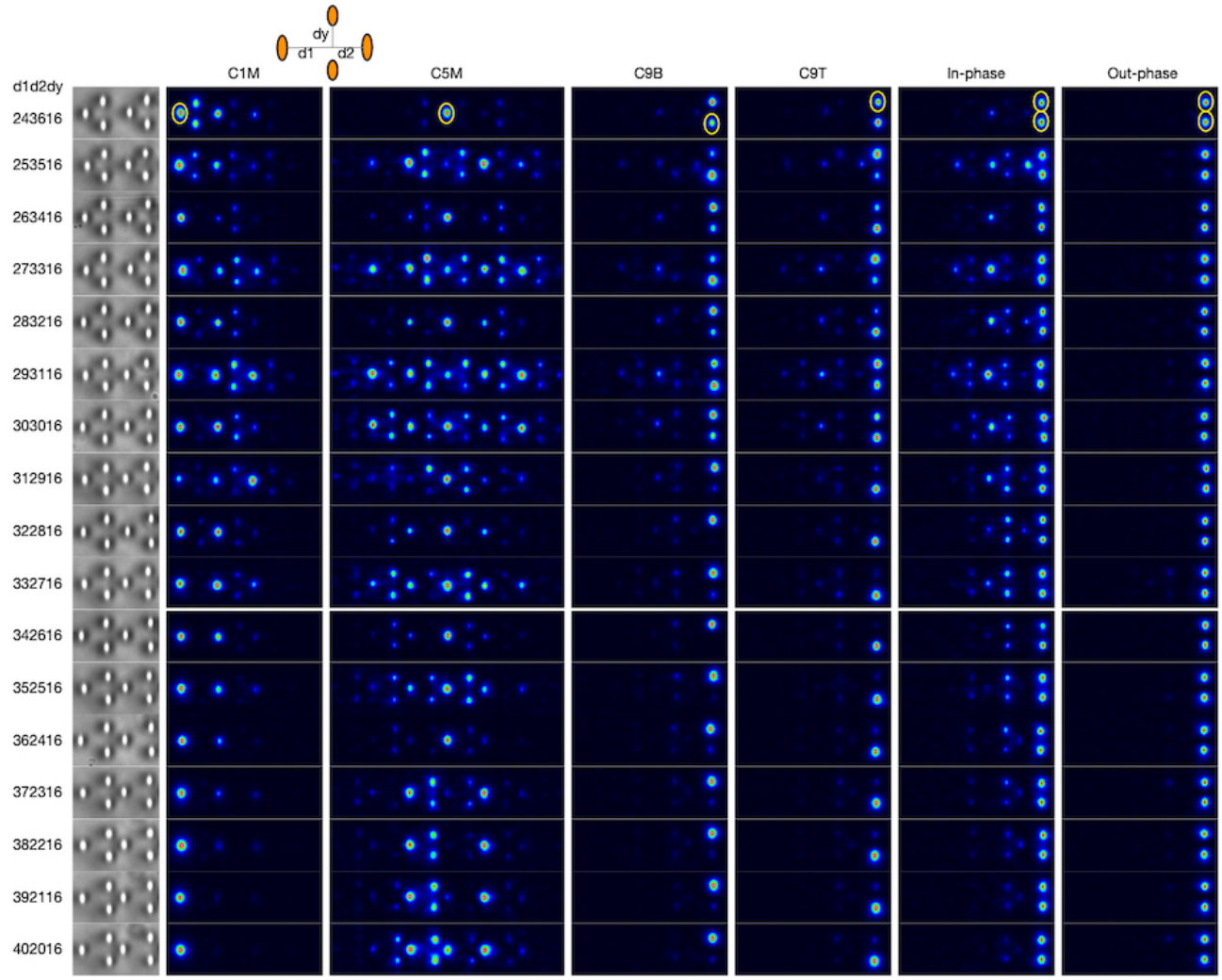

Figure S6. Experimental output images for different excitations, as indicated in the figure by yellow ellipses and upper text.

Topological edge states can be efficiently excited by injecting light directly into the waveguides located at the lattice boundaries, what naturally depends on the value of δ [6]. We perform the experiment on 17 lattices to unveil the edge state at the left boundary, which have amplitudes at B sites only. Figures S7(a)-left and (b)-red show the output intensity profiles of five dimerized lattices as examples. For $\delta \gtrsim 1$, we observe that the light spreads into the bulk with non negligible amplitudes at sites A and C, what confirms the absence of topological edge localization in trivial dimerized lattices. On the other hand, for lattices having a smaller value of δ, a single-waveguide excitation gives output profiles exhibiting a clear decaying tendency from the edge into the bulk, with intensities at B waveguides mostly and only negligible intensities at sites A and C. As this input condition excites simultaneously edge and dispersive states, clear edge localization is observed only when the edge mode is very well localized for smaller values of δ [see the cases $\delta = 0.37$ and $\delta = 0.25$ in Figs. S7(a)-left and (b)-red].

The excitation of the edge states at the right boundary requires a more complex input condition with two beams having equal amplitude and equal phase, such that we can match this profile closely. Figure S7(a)-right presents a set of output intensity profiles for different dimerized lattices. For $\delta \gtrsim 1$, the light stays mainly at the right edge, with a weak propagation towards the center of the lattice, but with clear nonzero intensities at B sites as an indication of the trivial topology. Remarkably, for smaller values of δ, the light intensity at B waveguides becomes negligible and the intensity profile is formed by A and C sites mainly. This profile decays exponentially into the bulk as shown in Figs. S7(a)-right and (b)-black.

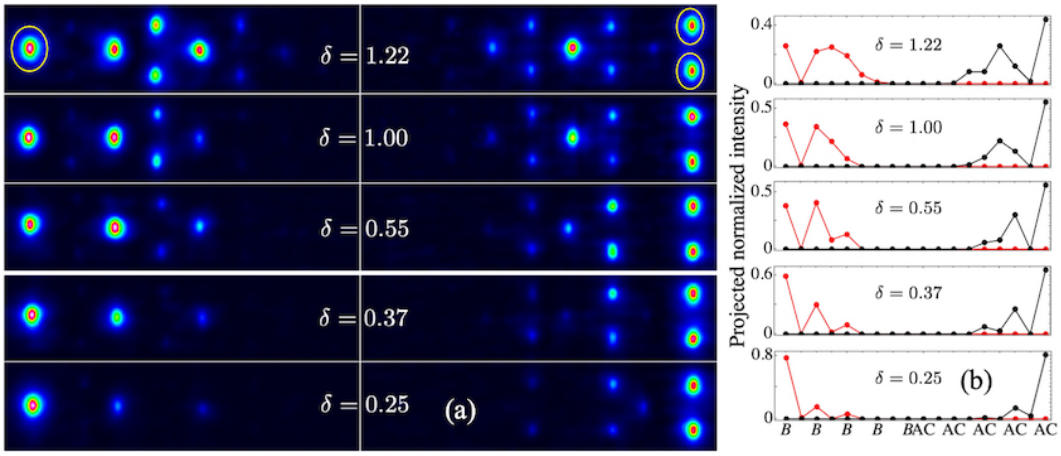

Figure S7. (a) Left and right intensity output profiles for a site B and in-phase A and C sites (see yellow ellipses), respectively, for five δ values. (b) Projected normalized intensity profiles: red for (a)-left and black for (a)-right images.

EXCITED SPECTRUM OF DIFFERENT INPUT CONDITIONS

To obtain numerically the excited spectrum of the dimerized diamond lattice, Eq. (1) of the main text is firstly solved, up to a given distance z_{max}, when considering a desired input condition. Thus, the light amplitude of every waveguide $\psi_n(z)$ is acquired in the interval $\{0, z_{max}\}$. Then, a discrete Fourier transform of the amplitudes along z is performed for every waveguide, giving the dynamically excited frequencies β_z for a given dimerizing parameter $\delta = t_1/t_2$. Figure S8 displays the excited spectra of several input conditions when sweeping δ in the interval $\{0, 2\}$. Panel (a) and (b) show that a single B and an in-phase AC input at the edges, respectively, excite the two topological edge states, together with extended states of dispersive bands. In contrast, an out-of-phase AC input at the right edge excites only the flat band, as shown by the straight black line at $\beta_z = 0$ in panel (c). The transport of the diamond lattice can be probed via the excitation of a B site in the bulk [see panel (d)], which excite only the two dispersive bands and allowed us to measure experimentally the averaged beam displacement shown in Fig. 2(c) of the main text.

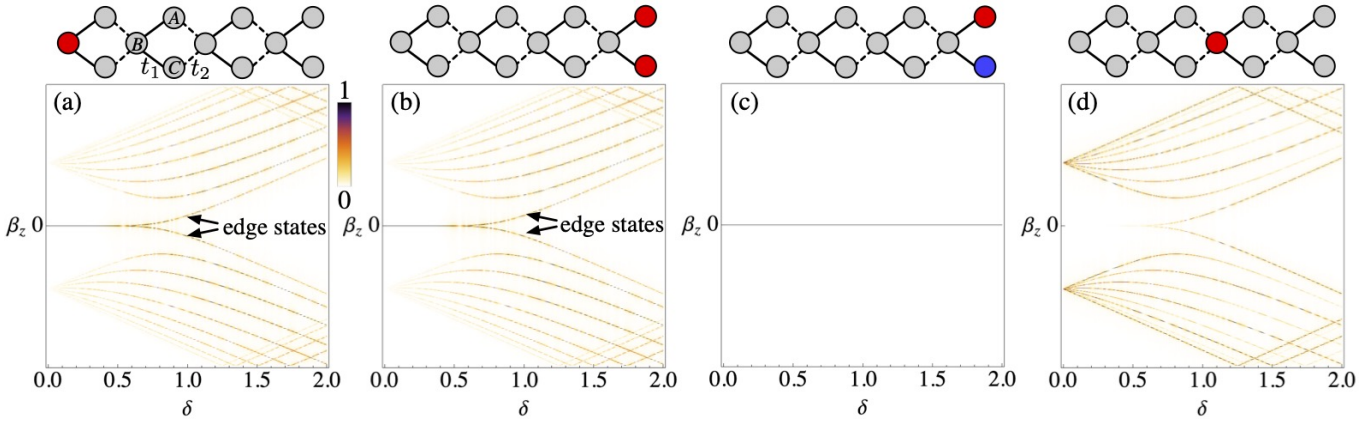

Figure S8. Numerical frequency spectra for different excitations. (a) Single B-edge, (b) in-phase AC-edge, (c) out-of-phase AC-edge and (d) single B-bulk input condition. Sketches on top depict the excitation in every case where red and blue colors denote the excited waveguides. In (c) blue waveguide represents an excitation with a phase difference of π respect to the red waveguide. Simulations were performed considering a dimerized diamond lattice composed by 9 unit cells and a propagation length of $z_{max} = 1000$. $\delta = t_1/t_2$ and $t_2 = 1$.

WAVELENGTH-SCAN METHOD AND COMPUTATION OF THE AVERAGED MEAN DISPLACEMENT

Figure S9 shows the output profiles after exciting the central B site in seven selected dimerized lattices with different values of δ (we run this experiment for the whole 17 lattices). The geometries selected are indicated at the top of this figure. The wavelength-scan method shows quite clearly the dynamical propagation at every lattice, this allows us to measure the averaged beam displacement for each case and extract the topological phase, as it is shown in Fig. 2(c) of the main text.

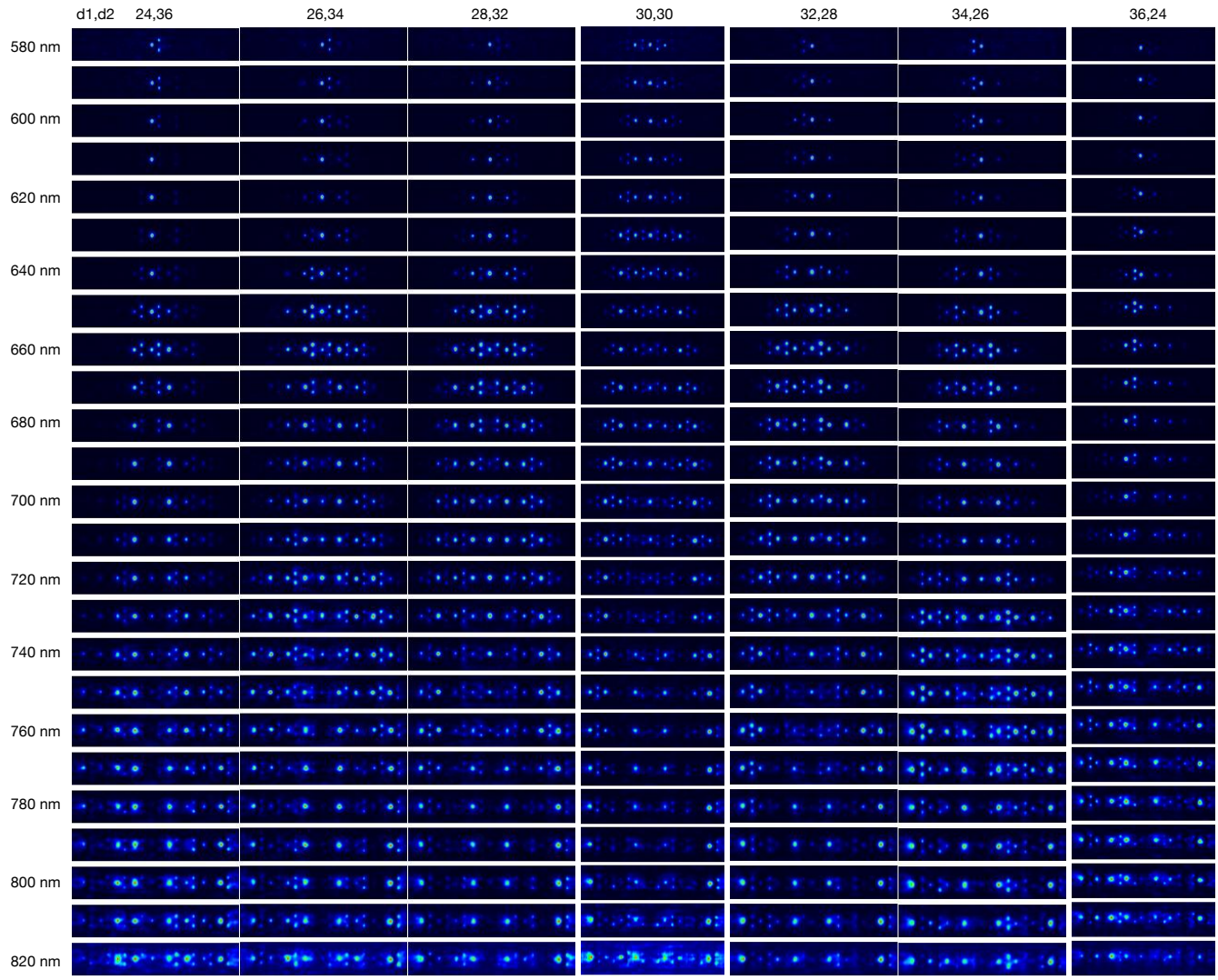

Figure S9. Output intensity profiles for a B central (5-th unit cell) excitation of dimerized diamond lattices with the geometry indicated at the upper text. Every row corresponds to a different input wavelength from 580 to 820 nm, in steps of 10 nm.

It has been reported that the averaged beam displacement can detect a quantized Zak phase of a lattice [1]. We define the averaged beam displacement as:

$$m_d(z_{max}) \equiv \frac{1}{z_{max}} \int_0^{z_{max}} n_c(z) dz \ , \tag{11}$$

with $n_c(z)$ the center of mass, defined in the main text as

$$n_c(z) \equiv \sum_n nP_n \equiv \sum_n n(|A_n(z)|^2 + |B_n(z)|^2 + |C_n(z)|^2) \ . \tag{12}$$

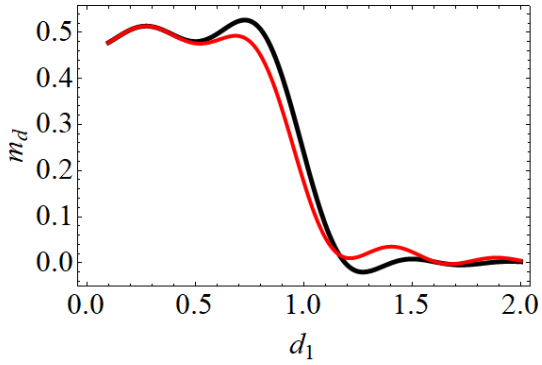

Figure S10. The computed averaged beam displacement for different δ. the black (red) line corresponds to simulations with 21 unit cells (9 unit cells) and $z_{max} = 10$ cm ($z_{max} = 5$ cm).

Let $\mathcal{Q}$ be the Zak phase, for large enough value of z_{max}, the averaged beam displacement approaches to $m_d = \mathcal{Q}/2\pi$ [1] giving the information of the Zak phase of the lattice. Therefore, we perform numerical simulations to observe this. Fig. S10 shows with a black line the averaged beam displacement for different δ using $z_{max} = 10$ cm and 21 unit cells, and with a red line for $z_{max} = 5$ cm and 9 unit cells. For the simulation we use a Kronecker delta type initial condition in the B site of the unit cell in the middle of the lattice. In the topological regime ($\delta < 1$) we observe that the averaged beam displacement is around $m_d = 0.5$ and the Zak phase in this region is $\mathcal{Q} = \pi$. This fulfills the condition $2\pi|m_d| = \mathcal{Q}$. On the other hand, in the trivial regime ($\delta > 1$) the averaged beam displacement is around zero as the Zak phase is also zero.

In order to observe experimentally the averaged beam displacement we use a supercontinuum laser source to excite the lattice. Generally, a change in the excitation wavelength λ changes the coupling between waveguides, for instance, as the wavelength increases, the couplings increase as well. Therefore, using the same lattice with different wavelengths we explore a larger region of couplings parameters. The increment in couplings is equivalent to a larger effective propagation length, thus we propose to measure the averaged beam displacement with respect the wavelengths.

Experimentally the camera takes a picture measuring the intensity in each pixel, the Figs. S11.(a)-(b) show the experimental output profiles of two lattices with different excitation wavelengths λ. As said before, the experiments were performed for 17 lattices but for this example we only use two cases, one for $\delta < 1$ and one for $\delta > 1$. The white lines in the middle of the pictures show the middle unit cell. We use the picture in black and white and the pixels value are a measure of the intensity, therefore we calculate the intensity in the n-th unit cell $P_n = |a_n|^2 + |b_n|^2 + |c_n|^2$ by adding the values of the pixels inside the n-th unit cell. Now, we calculate the center of mass $n_c = \sum_n nP_n$ from Eq. (12), and we want to compare it with respect the center unit cell. Fig. S11.(c) shows that the center of mass is around zero and this means that the excitation moves equally to the left than to the right. On the other hand, Fig. S11.(d) shows that the excitation moves to the left because the values are around $n_c = -0.5$. We use the images from $\lambda_{\text{min}} \approx 640$ nm to $\lambda_{\text{max}} \approx 750$ nm. λ_{max} is chosen for each lattice by observing that the excitation doesn't reach the edge and reflects, for instance in Fig. S11.(a) the excitation is just reaching the edge at $\lambda = 740$ nm. On the other hand, the λ_{min} is chosen by neglecting the images with low dispersion, for instance the first three pictures of the Fig. (S11).(a) shows very low dispersion. Finally, we calculate the averaged beam displacement m_d from Eq. 11 by calculating the average of the centers of mass n_c obtained from λ_{min} to λ_{max}.

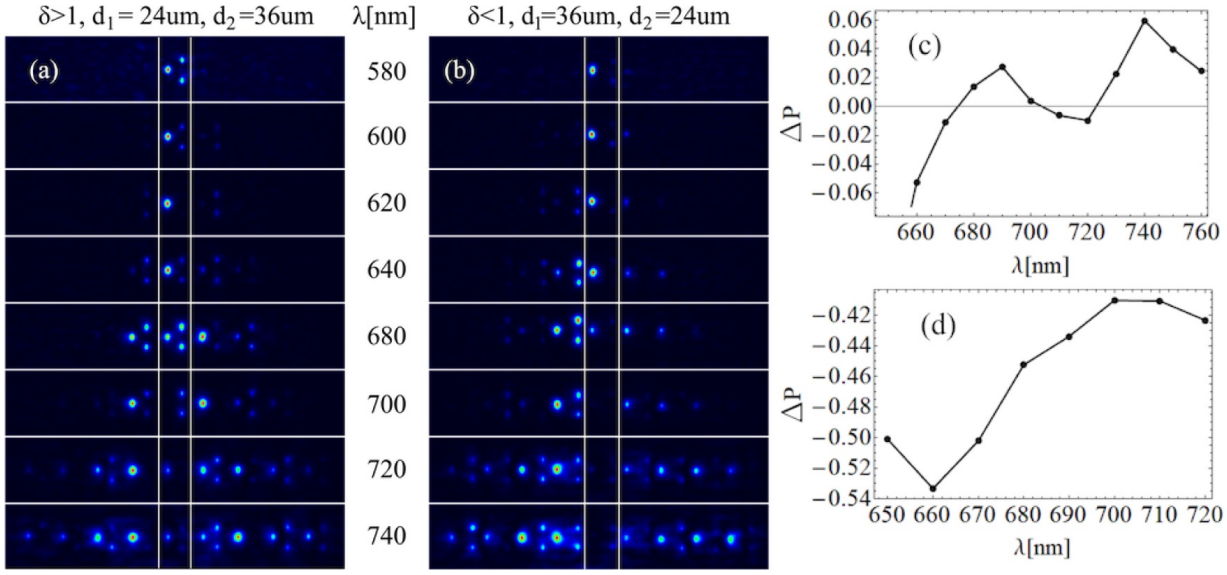

Figure S11. (a-b) Experimental Wavelength-scan images of the output face of samples with (a) $\delta > 1$ and (b) $\delta < 1$. The vertical white lines shows the middle unit cell. (c-d) Center of mass n_c calculated from the images in (a) and (b) respectively.

STATE TRANSFER BY EXCITING BOTH EDGES

In the main text, we demonstrated a spectral state transfer mechanism by exciting a B edge site. This is due to the similarity of the edge state at that border and the single B site excitation. However, the state transfer may occur at both borders as we show in Fig. S12 by exciting the B-edge site (upper images) and the C-edge site (bottom images). Naturally, a B excitation is cleaner in terms of exciting less the dispersive modes, while a C excitation is more uncoherent, because it excites FB and dispersive states too. Nevertheless, we clearly observe the state transfer mechanism in both cases, showing the applied possibilities of this effect.

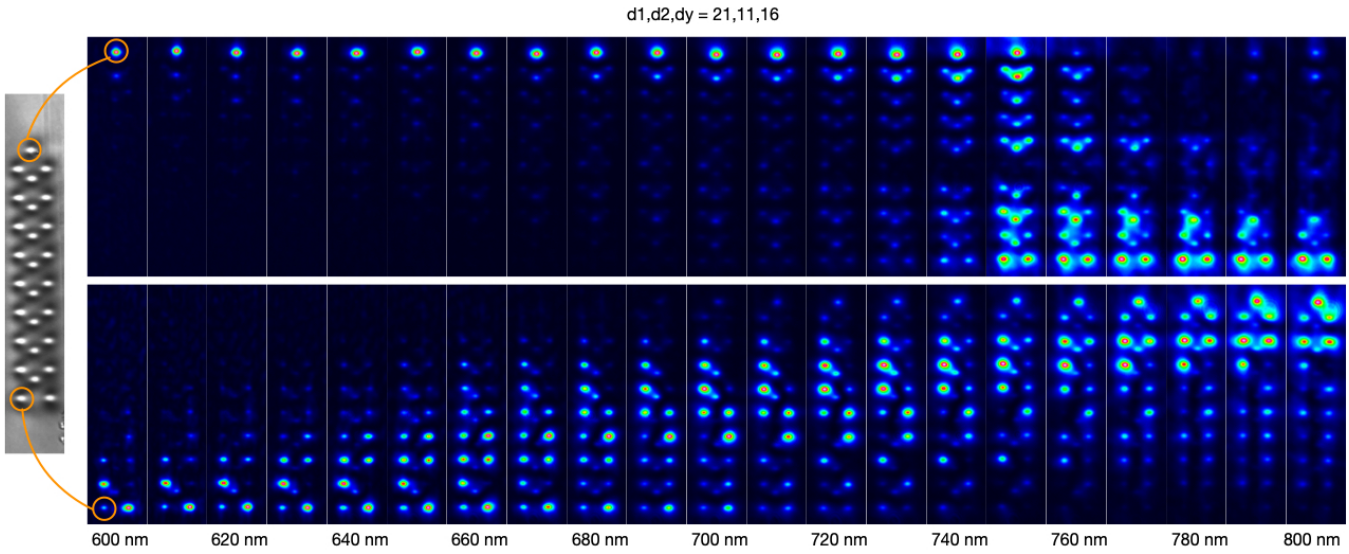

Figure S12. Wavelength-scan for a topologically nontrivial lattice ($\delta < 1$). Output intensity profiles for a B-edge (upper row) and a C-edge (bottom row) excitation of dimerized diamond lattice with $\{d_1, d_2, dy\} = \{21, 11, 16\}$ μm. The wavelength is swept in the interval 600 to 800 nm, in steps of 10 nm.

EFFECT OF IMPURITIES ON THE STATE TRANSFER

In this section, we show the results of the state transfer in different situations. We start by showing the state transfer for a topological lattice in the first column of Fig. S13. As said in the main text, these results differs from a common discrete diffraction in a trivial lattice (second column in Fig. S13), because the last one is a wave package that explores the hole lattice to travel to the other edge. The advantage of the topological edge to edge transfer is it's resilience to certain types of disorder. To check this, we fabricate four more lattices (two topological and two trivial) with a coupling defect. This defect consist in a larger separation between the central B site and his nearest neighbors, setting the horizontal distance to 23 μm. Also, in two of these lattices (one topological and one trivial) we change the writing power of the central B site, creating an impurity (site defect). We test these four lattices exciting the B edge site with different wavelengths, we show the results on Fig. S13. From these images we can claim that for trivial lattices, the ballistic transport explores the lattice completely and part of the energy is reflected back when interacting with this site defect. On the other hand, for topologically nontrivial lattices, the excitation is able to jump from one edge into the other, interacting weakly with these defects. This translates into more power on the other edge, which is an advantage for applications.

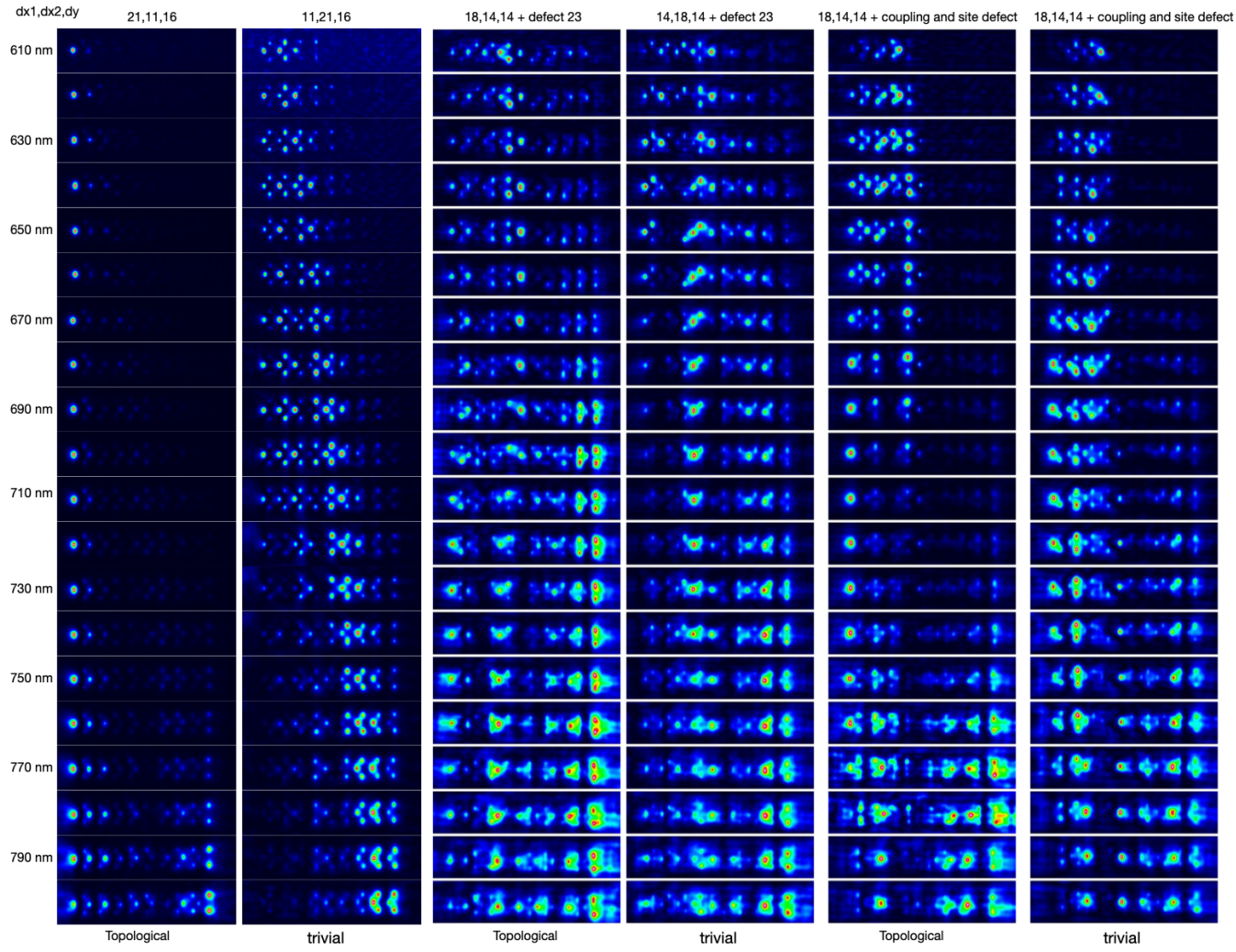

Figure S13. Wavelength-scan for topological ($d_1 > d_2$) and trivial lattice ($d_1 < d_2$) with different defects. Output intensity profiles for B-edge site excitation for different dimerized diamond lattices with distances d_1, d_2 and dy as indicated in each column. The wavelength was varied in the interval 610 to 800 nm, in steps of 10 nm.

[1] S. Longhi, Probing one-dimensional topological phases in waveguide lattices with broken chiral symmetry, Opt. Lett. **43**, 4639 (2018).
[2] R. S. Mong and V. Shivamoggi, Edge states and the bulk-boundary correspondence in Dirac Hamiltonians, Phys. Rev. B **83**, 125109 (2011).
[3] K. M. Davis, K. Miura, N. Sugimoto, and K. Hirao, Writing waveguides in glass with a femtosecond laser, Opt. Lett. **21**, 1729 (1996).
[4] A. Szameit, D. Blömer, J. Burghoff, T. Schreiber, T. Pertsch, S. Nolte, A. Tünnermann, and F. Lederer, Discrete nonlinear localization in femtosecond laser written waveguides in fused silica, Opt. Express **13**, 10552 (2005).
[5] D. Guzmán-Silva, G. Cáceres-Aravena, and R. A. Vicencio, Experimental observation of interorbital coupling, Phys. Rev. Lett. **127**, 066601 (2021).
[6] G. Cáceres-Aravena, B. Real, D. Guzmán-Silva, A. Amo, L. E. F. Foa Torres, and R. A. Vicencio, Experimental observation of edge states in ssh-stub photonic lattices, Phys. Rev. Research **4**, 013185 (2022).